FRICTION-STIR-WELDED AND SPIN-FORMED END DOMES FOR CRYOGENIC TANKS

S.J. Hales, W.A. Tayon and M.S. Domack
NASA Langley Research Center
Hampton, Virginia

ABSTRACT

Manufacturing of single-piece end domes for cryogenic tanks employing spin forming of tailored, friction-stir-welded blanks of Al-Li alloy 2195 plate offers cost and reliability benefits. The introduction of plastic deformation into a friction stir weld is a unique feature of the proposed manufacturing route. This investigation addressed abnormal grain growth [AGG] within the friction stir weldments during post-fabrication processing of a prototype dome. The phenomenon of AGG was observed during the solution heat treatment [SHT] phase of T8 tempering and is a major concern for meeting specifications. Such abrupt microstructural transitions can be detrimental to notch-sensitive mechanical properties, such as ductility and/or fracture toughness. If the issue of AGG cannot be resolved, then the acceptance of this approach as a viable manufacturing route may be in jeopardy. The innovative approach adopted in this investigation was the insertion of a stand-alone, Intermediate **A**nnealing **T**reatment [**IAT**] between the spin forming and T8 processing operations. A simple, recovery annealing step was deemed to be the most readily-scalable solution when fabricating thin-walled, ellipsoidal domes. The research effort culminated in the development of an effective IAT, which resulted in a significant decrease in AGG following SHT. The processing philosophy adopted in designing the IAT is outlined and the microstructural reasons for success are discussed. The analytical results presented are consistent with promoting continuous grain growth during the prior IAT, thereby suppressing AGG during the subsequent SHT.

INTRODUCTION

BACKGROUND

Manufacture of the forward and aft domes for the liquid hydrogen tank on the Space Shuttle employed traditional gore panel construction, as illustrated in ***Figure 1(a)***. Each section was stretch-formed to complex curvature, chem-milled, trimmed to shape, heat treated and then the panels were fusion welded together (1). Recently, a 5 meter diameter prototype dome was fabricated by combining friction stir welding [FSW] and single-piece, spin forming deformation [SFD] technology at MT Aerospace in Augsburg, Germany, ***Figure 1(b)*** (2). Size limitations on commercially available starting stock dictated that the SFD blank was two Al-Li alloy 2195 plates welded together. FSW of 2195 plate in various gages is flight-ready technology, being used during construction of the cylindrical sections on the Super Lightweight Tank [SLWT] (1). Considerable weight and cost savings have been realized by adopting the FSW/SFD combined process for the barrel sections. Further cost benefits are anticipated by using SFD technology to fabricate the end domes on next-generation cryogenic tanks.

The current thermo-mechanical processing profile for the proposed FSW/SFD manufacturing route is outlined in ***Figure 2***. Alloy 2195 has the nominal composition of Al-4.0Cu-1.0Li-0.4Mg-0.4Ag-0.1Zr [wt. %] and the starting material is 19 mm thick plate in the fully soft, O temper condition. Fabrication commences with FSW of two plates parallel to the prior rolling direction, followed by a stress relief annealing treatment. Subsequent machining operations produce a 5 m diameter, tailored blank with a varying radial thickness of 5 to 8 mm. Progressive SFD at warm temperatures gradually creates an ellipsoidal dome of uniform thickness [~ 2.5 mm]. The final stage of fabrication involves processing of the spin-formed article to the high-strength, T8 temper condition for service properties. The occurrence of AGG in weld nuggets has been a concern since FSW processing of alloy 2195 was first explored for reducing the cost of the SLWT (3).

(a) Current: Multi-piece assembly

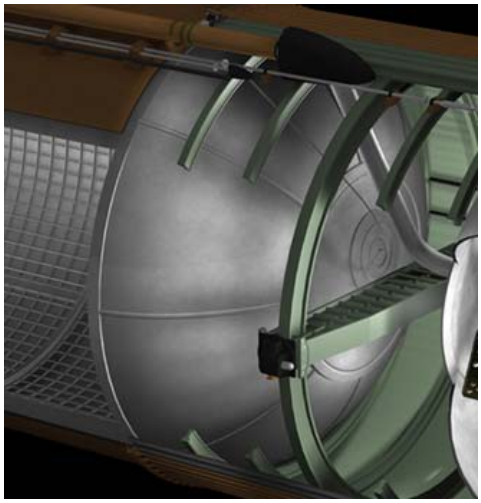

(b) Prototype: Single-piece construction

Potential Benefits:

Friction Stir Welding;
- No molten material
- Less welding defects
- Better mech. props.

Spin Forming;
- Reduced part count
- Reduced scrap rate
- Lower Fab. costs

Figure 1. Fabrication of the end domes for cryogenic propellant tanks: (a), multi-piece assembly used on the Space Shuttle (1); (b), single-piece construction approach proposed for future launch vehicles, combining Al-Li alloys with friction stir welding and spin forming technologies.

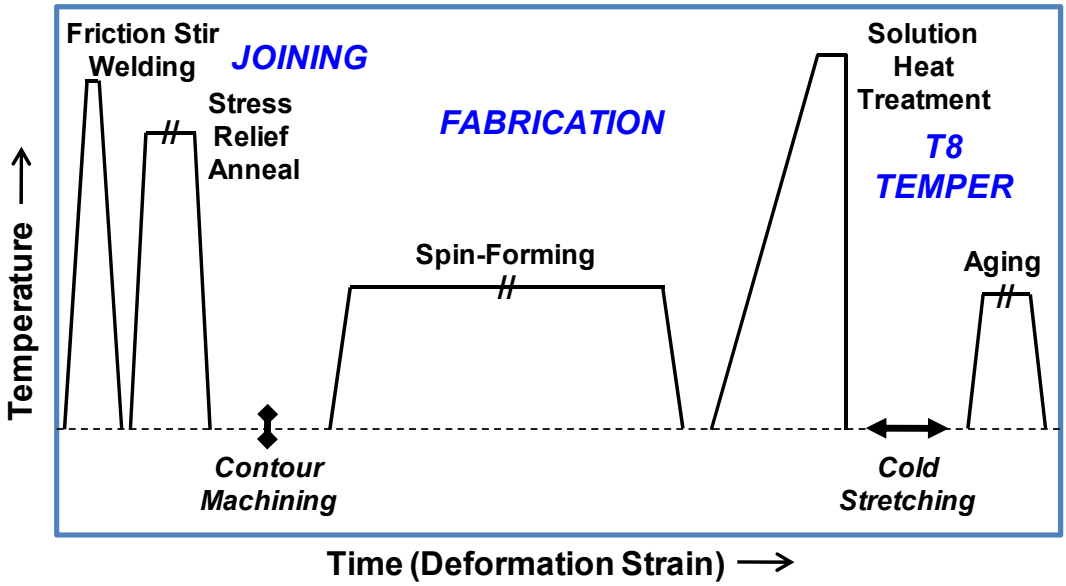

Figure 2. Thermo-mechanical processing profile for the manufacturing of Al-Li 2195 prototype end domes (2): FSW of 2 plates [plus machining] produces a large, circular blank; progressive spin forming operations create the ellipsoidal shape; T8 processing generates service properties.

A preliminary evaluation on 2195 material produced by FSW/SFD was conducted in earlier work (4). The effect of standard T8 tempering on the microstructure of a deformed weld nugget is illustrated in ***Figure 3***. The orientation of the full-penetration, butt weld with respect to a fabricated dome is indicated beside the micrographs. It is worth outlining the anatomy of a typical friction stir weld at this juncture. The weldment consists of the weld nugget, bordered on both sides by thermo-mechanically affected zones [TMAZ's]. These represent microstructural transitions from the characteristics of the weld nugget back to those of the parent metal. The advancing side [at left] exhibits an abrupt change in microstructure at the nugget/TMAZ interface. In contrast, the retreating side [at right] shows a more gradual shift within the TMAZ region. The

weld crown side [at top], and the weld root side [at bottom], correspond to the outer and inner mold lines of a fully-fabricated article, respectively. Note that the actual crown and root locations of the weld nugget were removed during the contour machining stage, prior to spin-forming operations.

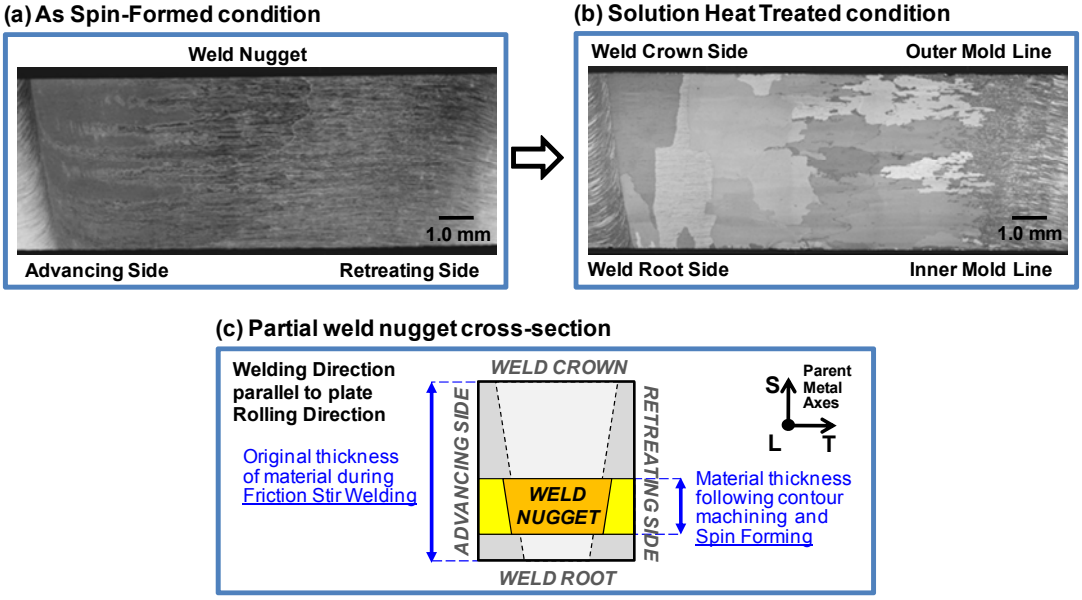

Figure 3. AGG in a deformed weld nugget during standard T8 processing of Al-Li 2195: (a), as spin-formed condition; (b), solution heat treated condition; (c), schematic of friction stir weld cross-section remaining after contour machining and spin forming operations.

The undesirable AGG during the SHT phase of conventional processing has transformed a heavily deformed microstructure with indistinct features [***Fig. 3(a)***] into a very coarse-grained structure [***Fig. 3(b)***]. It is evident that some grain boundaries extend through the entire section thickness [primarily on the advancing side]. In both micrographs, the tortuous line weaving through the center of the weld nugget is a remnant of the faying surface from the original butt joint between the two plates. The accompanying schematic [***Fig. 3(c)***] shows the size and approximate location of the remaining weld nugget with respect to the dimensions and orientation of the starting plate. The thickness of the spin-formed material being evaluated comprises only 25% of the original plate gage, due to prior contour machining and SFD operations. Note that a fully-formed dome would have a uniform thickness of ~ 2.5 mm from the 'pole' to the' rim' sections. The material evaluated in this study was from a partially formed dome where SFD operations were interrupted at a gage of ~ 5.0 mm in the intermediate 'membrane' section.

AGG MITIGATION

Although a concise description of the AGG phenomenon does not exist, it is widely recognized that it falls under the realm of secondary recrystallization [RX]. It may be categorized as an extreme example of a discontinuous grain growth [DGG] process, involving the very rapid growth of a very limited number of pre-existing grains (5). There are three principal differences between AGG and the mechanisms commonly associated with primary RX (6). First, there is no nucleation of new grains involved. Second, the process occurs within a fully recrystallized microstructure. Third, stored energy is primarily decreased by a reduction in the total grain boundary area. It is accepted that the mechanism is promoted by microstructural heterogeneities, such as localized variations in deformation strain, crystallographic texture, grain size, grain orientation, and boundary misorientation. Microstructural conditions which favor the growth of isolated grains at the expense of adjacent grains can include any combination of these factors. Consequently, there exists a multitude of possibilities for stabilizing a grain structure with respect to suppression of AGG (7).

In this case study, the weld nugget dynamically recrystallized during the FSW process and then was further plastically deformed. The characteristics of the grain structure following dynamic RX alone will be more complicated than those resulting from static RX, i.e. concurrent temperature and deformation effects (5). The intention of the current work was to use thermal processing to replace the inhomogeneous, coarse-grained microstructure with a uniform, refined grain structure. As shown in ***Figure 4***, the mechanism of DGG generally involves extensive migration of a few, high-angle grain boundaries [HAGB's]. In contrast, the mechanism of continuous grain growth [CGG] involves uniform microstructural coarsening via development and migration of many HAGB's (6). The CGG process also includes recovery-type mechanisms and substructure development, i.e. the formation, coalescence and migration of low-angle grain boundaries [LAGB's] (8). Therefore, the approach adopted was to promote CGG during a prior IAT, in order to reduce the stored energy for AGG during subsequent SHT.

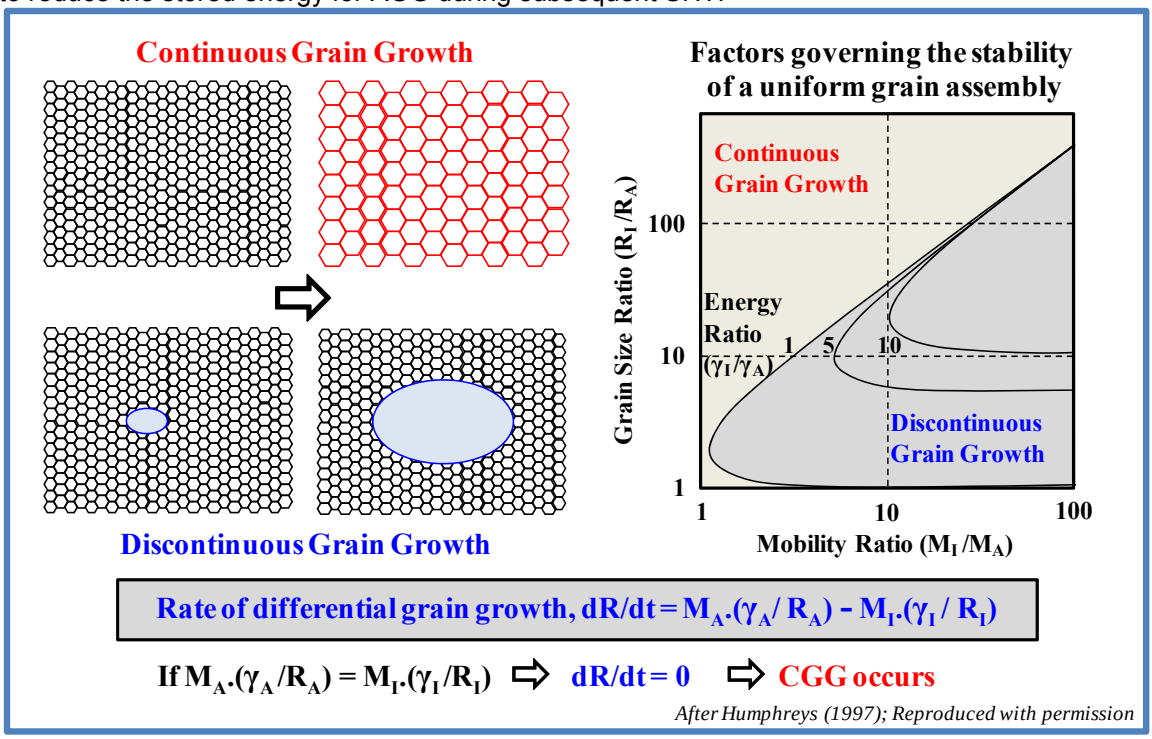

Figure 4. Microstructural stability depends on the grain radius [R_i], boundary energy [γ_i], and boundary mobility [M_i] of an Isolated grain, relative to the whole Array of grains. The primary objective was to suppress AGG by decreasing the $M_A.(\gamma_A/ R_A)$ term. Illustration adapted from the Humphreys model (9).

A unified model proposed by Humphreys is readily applicable to AGG suppression in a high solute, multi-phase Al alloy which has undergone complex, plastic deformation. The concepts developed blend existing theories of recovery, recrystallization and grain growth, and explain relative contributions to microstructural development. Specifically, the effect on DGG of factors such as strain energy, grain size, preferred texture, microstructural heterogeneities and precipitates have been considered (9)(10)(11). The basic model, addressing the stability of cellular microstructures, is summarized in ***Figure 4***. Control of microstructural conditions such that CGG is favored over DGG is the main principle. The model indicates that DGG can be suppressed if the growth advantage of a few, unstable grains can be eliminated. The controlling factors are presented in terms of the ratio in grain size, boundary energy and boundary mobility between isolated grains and the surrounding grain array. The details reveal that if $(M.\gamma/R)_A = (M.\gamma/R)_I$, then the rate of DGG is zero, i.e. CGG occurs [where: M ≡ boundary mobility; γ ≡ boundary energy; R ≡ grain radius, and A ≡ array of grains; I ≡ isolated grain]. From a practical perspective, this goal can be accomplished most readily by increasing R_A, thereby decreasing the

value of the $(M.\gamma/R)_A$ term. Hence, the thermal processing philosophy adopted in this study was to reduce the grain size differential by promoting CGG, thereby eliminating the growth advantage and suppressing DGG.

PROCESSING PHILOSOPHY

From a practical perspective, AGG tends to occur rapidly because it is a preferential growth process only. Consequently, the phenomenon tends to be more sensitive to absolute temperature than heating and cooling rates. It is generally accepted that there is a threshold temperature [T_{AGG}], below which AGG does not occur (8). T_{AGG} has been shown to be dependent on many factors, including alloy composition, strain rate, deformation strain and the nature of the stored energy. In this case, T_{AGG} will be affected by both the FSW and SFD parameters employed, and the varying levels of forming strain. Therefore, the approach adopted in this investigation combined microstructural stability concepts with traditional processing protocols and the influence of systematic microstructural gradients. The novel aspect of this work is that it addresses suppression of AGG within a deformed FSW weld nugget. This feature separates the current study from most of the open literature and existing patents, which tend to cover heat treatment of as-welded material only, and include analysis of whole nugget cross-sections.

There have been two important pieces of prior thermal processing research which are helpful to the present study. The first, shown in ***Figure 5***, was the work performed by Alcoa in an attempt to improve the mechanical isotropy of Al-Li alloy rolled products (12). The thermo-mechanical processing scheme developed [***Fig. 5(a)***] is compared with the partial Al-Cu phase diagram [***Fig. 5(b)***]. The binary diagram can be employed as a convenient temperature guide because the dominant solute in alloy 2195 is 4 wt.% Cu (7). The unusual step of correlating these data permits identification of the temperature regimes where microstructural changes are typically implemented using traditional processing protocols. SHT [~ 510°C] is conducted in the quasi-single phase region [non Cu-containing precipitates, such as Al_3Zr, are not included]. Recrystallization heat treatments [~ 490°C] are conducted close to the solidus temperature and hot working operations in the temperature regime immediately below [400-475°C]. Performing conventional recovery annealing treatments within the 250-400°C temperature range is of particular significance to this investigation.

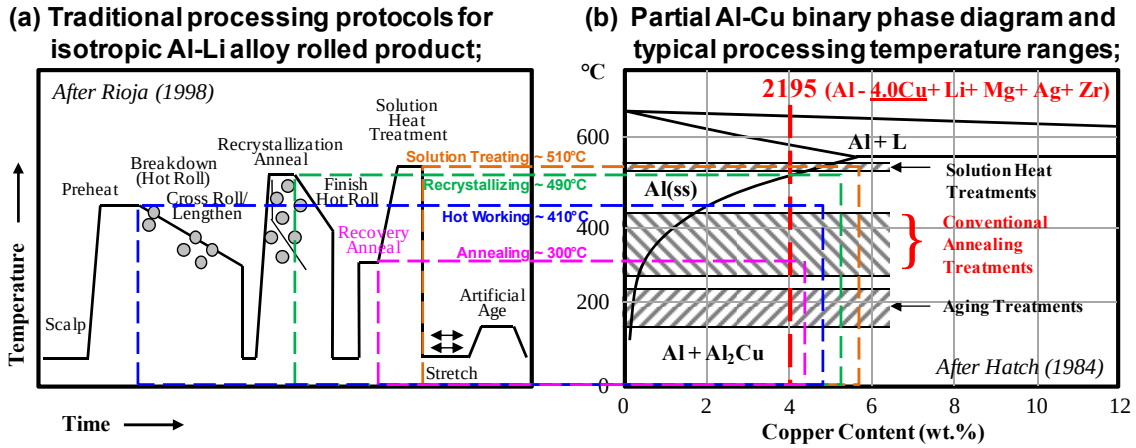

Figure 5. Establishment of typical thermal treatment practices for alloy 2195 materials: (a), thermo-mechanical processing profile for Al-Li alloy wrought product (12); (b), partial Al-Cu phase diagram, highlighting temperature regimes for different heat treatments (7).

The second significant piece of work was performed by Alcan to eliminate AGG during SHT following FSW 7xxx series Al alloys (13). Particle pinning concepts were adopted for microstructural stabilization; the aim was to modify the size and distribution of Al_3Zr dispersoids. The approach involved the application of prolonged anneals [≤ 72 hrs] at temperatures very close to the SHT temperature. The 'annealing' temperature was necessarily high because Al_3Zr is a

high melting point phase and the very long annealing times accounted for the thermal stability of the dispersoids. In this case study, the Alcan approach was considered applicable to post-FSW thermal processing only, as the exposure of deformed weldments to highly elevated temperatures would cause AGG. This implies that the IAT temperature selected needs to be higher than conventional recovery temperatures, but lower than the T_{AGG}. Accordingly, results from the combined studies were employed to define the upper and lower limits for the annealing temperature, and to bracket the scope of the annealing times evaluated.

EXPERIMENTAL

The material used in this study was extracted from the same location in the prototype dome for all of the processing and microstructural evaluations. Thermal treatment procedures conformed to current, commercial guidelines, e.g. temperature control margins, heating rates, soak times, cooling rates and furnace atmospheres (14). The longitudinal direction [L] is parallel to both the rolling direction [RD] and the welding direction [WD]. The size of the heat treat coupons was such that the smallest dimension corresponded to the short-transverse [S], or through-thickness, direction in the weld nugget, i.e. width [// FSW; // L] ≥ 2X thickness [⊥ FSW; // S]. As a consequence, any 'free-surface' effects on AGG behavior, and the resultant microstructure, would be comparable with processing of full-scale domes (6). The initial objective of the IAT studies was to establish T_{AGG}. The first series of heat treatments performed were of short duration [1 hr], because AGG occurs very rapidly. Subsequent heat treatment studies were conducted at a temperature suitably below T_{AGG} in order to establish the annealing time. The second series of heat treatments performed were of practical duration for an effective IAT, considered to be between 12 and 72 hours.

Specimens for metallurgical analyses were sectioned perpendicular to the weldment at the mid-plane of heat treated coupons, i.e. plane as remote from the free surfaces as possible. Qualitative optical metallography [OM] of the entire weld nugget cross-section was conducted during the IAT design studies. Two standard specimen preparation/ imaging mode combinations were employed; Keller's chemical etching/ bright field [K/BF] images and Barker's electro-chemical etching/ cross-polarized [B/XP] images. Once the best annealing temperature and time for the IAT had been identified, electron back-scattered diffraction [EBSD] techniques were employed along a diagonal traverse of a weld nugget. Quantitative metallurgical analyses concentrated on the differences in [sub]grain structure, microtexture and [sub]grain boundaries between 'the start' and 'the end' of the most effective IAT. First, OM images were collected contiguously across a nugget and then EBSD analyses were conducted on the same samples. This was to ensure that data gathered from limited area was representative of the bulk microstructure. In both cases, quantitative metallography practices were in conformance with ASTM specifications (15)(16). Measurements were conducted along a diagonal traverse of the weld nugget to capture the contribution of both horizontal and vertical microstructural gradients.

RESULTS

THERMAL PROCESSING STUDIES

A selection of the extensive K/BF micrographs collected in order to arrive at an effective IAT design is shown in ***Figure 6***. The annealing temperature [***Figs. 6(a)-(d)***] and the annealing time [***Figs. 6(e)-(h)***] were derived empirically in separate studies. Note that the material is in the intermediate annealed condition only in ***Figs. 6(a)-(d)***, and has not been exposed to the SHT temperature. Progressively increasing the temperature for the 1 hour soak from $\mathbf{T_1}$ to $\mathbf{T_4}$ by equal increments revealed that T_{AGG}= $\mathbf{T_4}$. The highest annealing temperature for the shortest duration was the original goal. A suitable buffer to allow for furnace variations and scale-up to large parts was also desirable. Therefore, a recovery annealing temperature of $\mathbf{T_3}$ was selected for the IAT. This may be considered a 'non-conventional' annealing temperature in the sense that it is in the regime that is normally reserved for RX heat treatments and/or hot working operations [***Figure 5***]. The second study was used to identify the appropriate annealing time, and the number of

iterations was reduced by down selecting the T_3 annealing temperature only. Note that the material is in the 'IAT + SHT' condition in ***Figs. 6(e)-(h)***. The series of images reveal that the substantial areal fraction of oversized grains after exposure for $\square_1$ hours was essentially reduced to zero following $\square_4$ hours. Progressively increasing the duration of the recovery annealing treatment gradually reduced AGG until the reaction was effectively suppressed. Consequently, a recovery annealing time of $\square_4$ hours was selected as the most promising for the IAT.

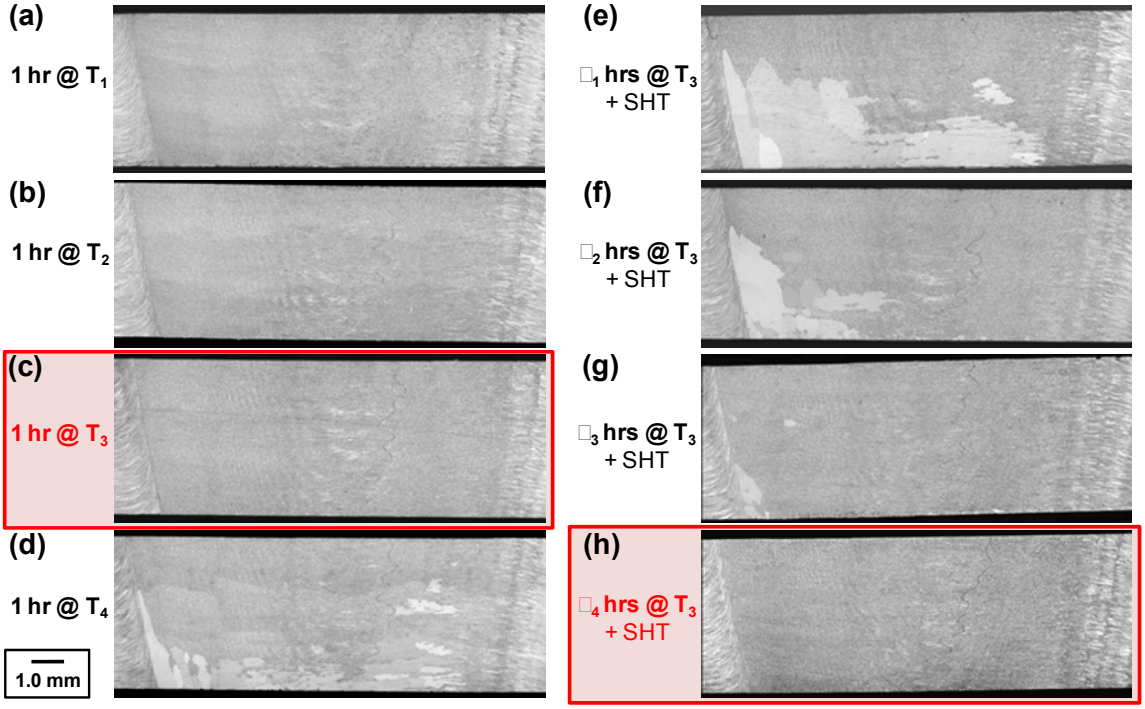

Figure 6. Definition of parameters for an effective IAT [$\square_4$ hrs at T_3] : Figs.(a)-(d), the annealing temperature [$T_1 < T_2 < T_3 < T_4$; $T_4 = T_{AGG}$], material in 'IAT only' condition; Figs.(e)-(h), the annealing time [$\square_1 < \square_2 < \square_3 < \square_4$], material in 'IAT + SHT' condition.

The microstructural changes occurring during the best IAT are represented on a broad scale by the B/XP images shown in ***Figure 7***. The characteristics of the nugget cross-section after 1 hour at T_3, the 'Start of the IAT' [***Fig. 7(a)***], and following $\square_4$ hours at T_3, the 'End of the IAT' [***Fig. 7(b)***], can be compared. The images exhibit very similar characteristics with few visible differences. The IAT has resulted in a general sharpening of the contrast and the emergence of a scattering of small grains along the weld root side. In both micrographs, a common characteristic of FSW weld nugget microstructures, i.e. the onion rings, is revealed by the different preparation technique (17). The rings are so well-defined because B/XP imaging relies on crystallographic orientation contrast. The banding of grains with differing orientation has been associated with the varying intensity and directionality of shear deformation created during the FSW process (18). As documented in the earlier work, these features are primarily a product of spatial variations in texture and grain morphology, rather than grain size *per se* (4).

The series of micrographs showing a progressive reduction in AGG with annealing time, ***Figs. 6(e)-(h)***, reveal a persistent trend. There is a preponderance of oversized grains adjacent to the intersection between the advancing side interface and the root side of the partial weld nugget. As a result, ***Figure 8*** serves to illustrate the incorporation of previously documented microstructural gradients in friction stir welds into the quantitative EBSD analysis of the reduced weld cross-section. Earlier reports on whole nuggets document systematic strain gradients from both the advancing side [AS] to the retreating side [RS] (17), and from the root [R] to the crown [C] sides of weldments (19). Non-symmetrical variations in grain size/morphology and crystallographic texture have also been noted, the nature of which tend to depend on FSW parameters (20). The

schematic in ***Figure 8(a)*** combines these findings and outlines the working hypothesis for the analytical approach adopted in this case study. Quantitative metallurgical analyses were conducted using a diagonal line connecting the 'AS -Root' [A_R] and 'RS-Crown' [R_C] intersections, i.e. along 'A_R to R_C' traverses of the deformed weld nugget.

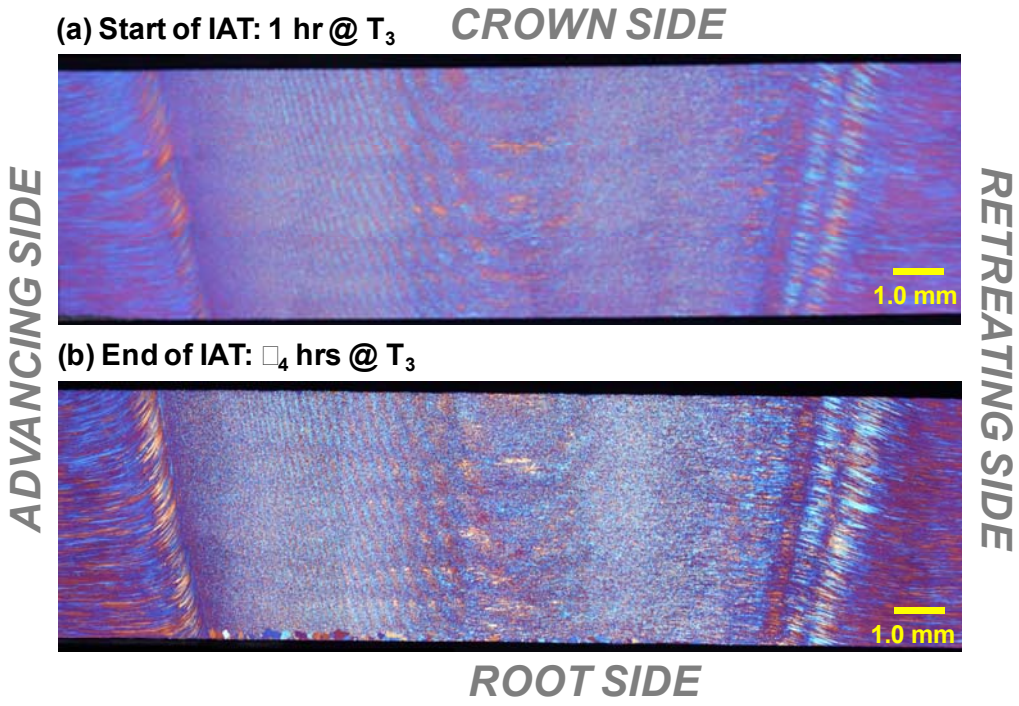

Figure 7. Microstructural characteristics revealed by combination of Barker's etching and cross-polarized light imaging of spin-formed, partial weld nuggets: (a) at the beginning of the IAT; (b) at the conclusion of the IAT.

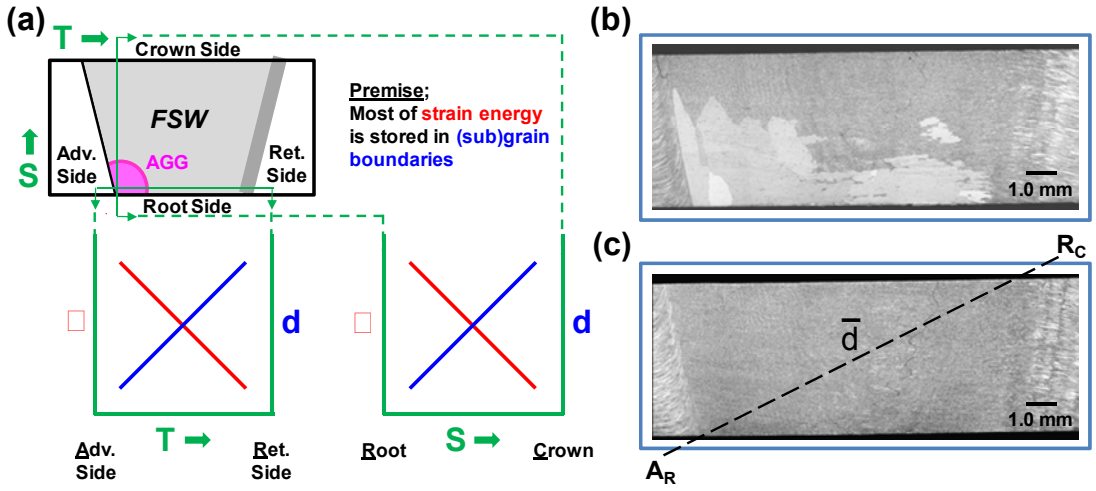

Figure 8. Inclusion of gradients from FSW into EBSD analysis of a spin-formed weld nuggets: (a), schematic of working hypothesis developed; (b), 'SHT only' condition – typical location of AGG; (c) 'IAT only' condition – measurements along diagonal traverse.

The grain size following primary [static] RX tends to be inversely proportional to the level of stored strain energy (6). Accordingly, it may be inferred that a similar scenario exists for the complicated case of dynamic RX during the FSW process. The location-dependent balance between work and heat input within the weld nugget will be manifested in variations in the final grain size of the

fully-recrystallized microstructure (20). Combining this notion with the premise that most stored energy is contained in grain boundaries constitutes the hypothesis developed. The prevalence of AGG at the A_R location is illustrated most clearly in ***Figure 8(b)***, where large grains predominate on the root side and extend further into the weld nugget on the advancing side. Application of these concepts is summarized in ***Figure 8(c)***, showing material in which AGG has been suppressed. The location of a typical 'A_R-R_C traverse', along which quantitative EBSD analysis was performed, is shown.

QUANTITATIVE MICROSTRUCTURAL ANALYSES

The various types of data generated via EBSD analysis along A_R-R_C traverses are illustrated in ***Figure 9***, using the A_R location as an example. ***Figure 9(a)*** shows the use of inverse pole figures [IPF's] and IPF maps to determine the frequency and spatial distribution of microtextural components, respectively. The data can be interpreted as [sub]grain orientation information and can be transformed such that RD/WD [// L] becomes the reference axis, rather than the traditional ND [// S]. Note that the term [sub]grain is used to denote the crystallites within an aggregate when the distinction between 'subgrains' and 'grains' is not drawn. Furthermore, the IPF data can be reduced to permit comparison with the texture characteristics common in Al-Li alloy wrought product. The large quantity of data produced can also be exploited to quantify the statistical distribution of the sizes and boundary misorientations of [sub]grains. ***Figure 9(b)*** shows the [sub]grain area distribution information extracted. It is evident that the distribution is approximately log-normal and is a consistent observation at all of the locations analyzed. Similarly, ***Figure 9(c)*** shows the that the [sub]grain boundary misorientation distribution differs from that of a random polycrystalline aggregate (21). The distributions intersect at a boundary misorientation, θ, of ~ 30°. The frequencies for θ>30° boundaries are lower [HAGB's], and that for θ<30° boundaries are higher. It should be noted that this latter category contains all the LAGB's associated with subgrain structure, i.e. θ<15°. This observation proved to be common in the microstructure at all locations evaluated, and is indicative of the level of substructure present.

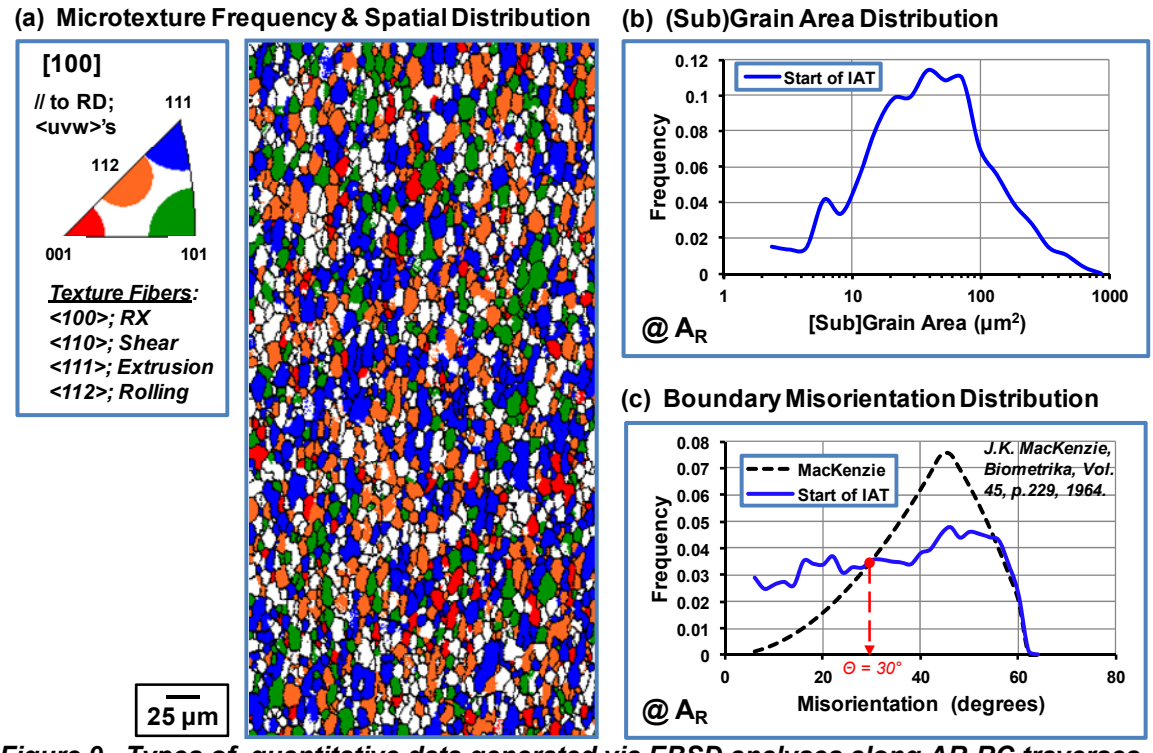

Figure 9. Types of quantitative data generated via EBSD analyses along AR-RC traverses of deformed weld nuggets [using AR location as an example]: (a) preferred [sub]grain orientations; (b) average [sub]grain dimensions; (c) [sub]grain boundary misorientations.

The frequency of preferred [sub]grain orientations is represented by the variation in areal fraction of common texture fibers along the A_R-R_C traverse in ***Figure 10***. The information allows the textural composition of the material at the start [1 hour @ T_3] and end of the IAT [□4 hours @ T_3] to be compared and contrasted. Note that texture fibers are generally families of {hkl}<uvw> crystallographic orientations with a common <uvw> or {hkl} component (22). Specific to FSW of Al alloys torsional deformation results in the emergence of so-called A-{111}<uvw> and B-{hkl}<110> fibers and the C-{001}<110> component. It is noteworthy that such dynamically recrystallized microstructures have also been shown to exhibit a higher fraction of LAGB's (23). In Al-Li wrought product, the <100>-fiber is typically associated with static recrystallization [RX], even though the microstructures tend to be predominantly unrecrystallized. The presence of <110>-, <111>-, and <112>-fibers is common, and formation can be related to the type of deformation encountered (24). The <110>- and <111>-fibers are related to pure shear, and mixed shear deformation conditions, respectively. The <110>-fiber is also observed in many wrought materials (22), and the <111> fiber tends to dominate in Al-Li extrusions (25). The <112> fiber is often referred to as a 'skeleton line' of ideal crystallographic orientations, but it is in close proximity to the β-fiber frequently formed in Al alloy rolled products (26).

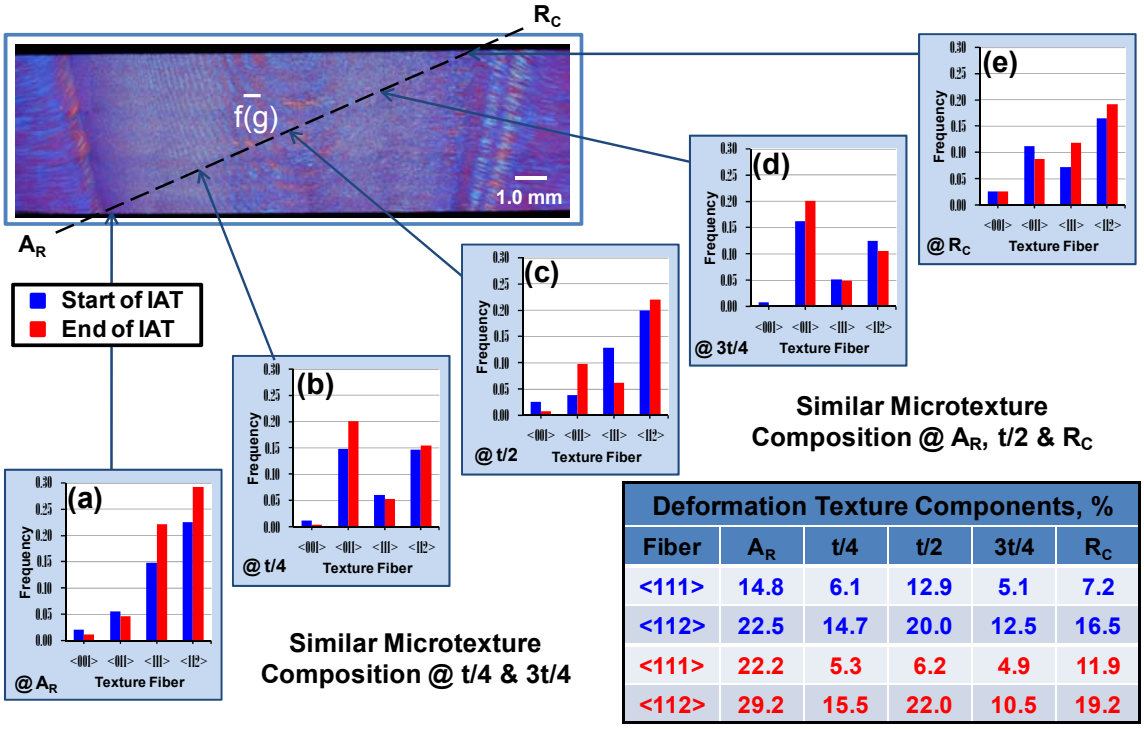

Deformation Texture Components, %					
Fiber	A_R	t/4	t/2	3t/4	R_C
<111>	14.8	6.1	12.9	5.1	7.2
<112>	22.5	14.7	20.0	12.5	16.5
<111>	22.2	5.3	6.2	4.9	11.9
<112>	29.2	15.5	22.0	10.5	19.2

Figure 10. Effect of IAT on microtexture distribution along A_R-R_C traverse of deformed weld nugget: Figs.(a)-(e) show relative contribution of selected texture fibers. Two distinct microtexture compositions, and IAT causes subtle changes only.

The microtexture data indicate that the texture along the A_R-R_C traverse may be divided into two distinct compositions. Although varying in intensity across the weld nugget, the textural composition at the A_R, t/2 and R_C locations is similar, i.e. the <112>-fiber makes the largest contribution [***Figs. 10(a), (c), &(e)***]. Likewise, the texture characteristics at the t/4 and 3t/4 locations are similar, but of a different composition, i.e. the <110>-fiber contributes the most [***Figs. 10(b) &(d)***]. The IAT does seem to have a subtle effect on texture composition within the two distinct categories. However, caution is exercised in interpretation of this data because of the fluctuations introduced by the onion ring features [***Fig. 7***]. The tabulated data [inset] highlights both the cross-sectional variation in, and the effect of the IAT on, two of the more prominent fibers noted. These may be significant because <111> and <112> provide the highest contribution at

the A_R location and it appears to increase during the IAT. It may be surmised that subtle shifts in (sub)grain orientation reduce the growth advantage of certain grains residing in the region where AGG is the most prevalent.

The EBSD data was also employed to generate the statistical distribution of [sub]grain areas along the A_R-R_C traverse presented in ***Figure 11***. The effects of variability in [sub]grain size and morphology noted in earlier work (4), by determining L, T, and S dimensions via mli methodology, can be reduced in this manner. The series of plots also show that the grain area distribution is approximately log-normal throughout the cross-section. Of significance, the distribution appears to be narrower at the A_R and t/4 locations and the IAT has resulted in further sharpening [***Figs. 11(a) &(b)***]. The distribution does appear to be broader [peak height marginally lower] at other locations [***Figs. 11(d) &(e)***] and particularly at t/2 [***Fig. 11(c)***]. Again, caution should be exercised in interpretation of this data because of fluctuations potentially introduced by the onion rings.

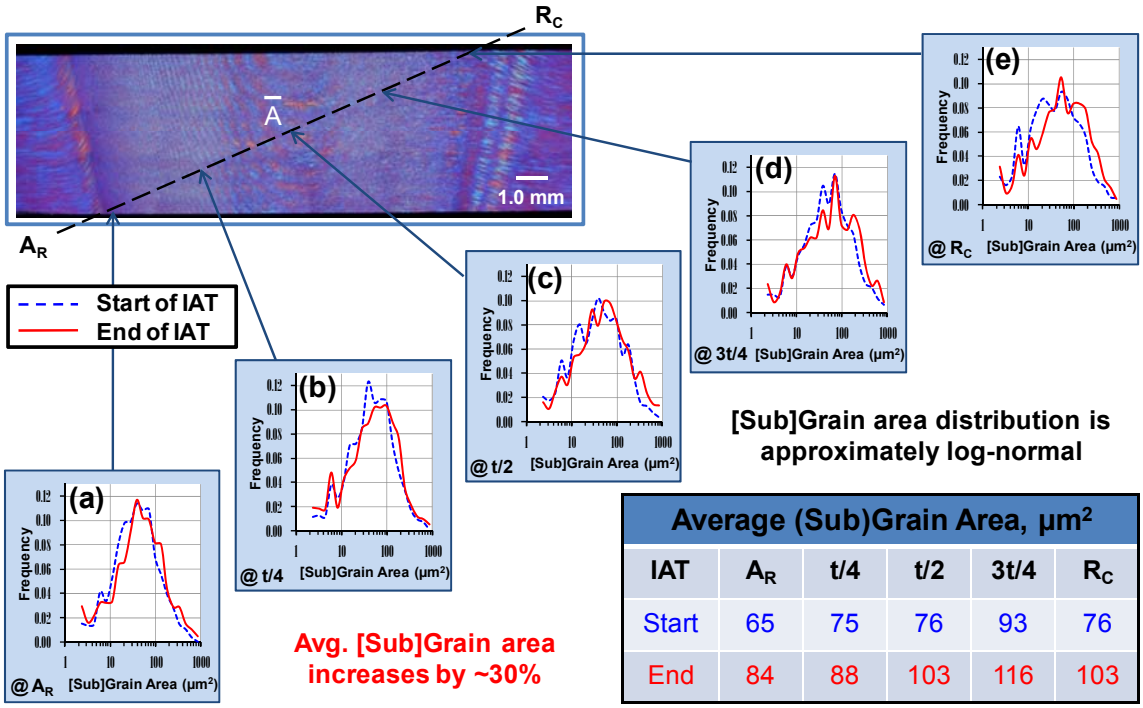

Average (Sub)Grain Area, μm²					
IAT	A_R	t/4	t/2	3t/4	R_C
Start	65	75	76	93	76
End	84	88	103	116	103

Figure 11. Effect of IAT on [sub]grain area distribution along A_R-R_C traverse of deformed weld nugget: Figs.(a)-(e) show approximately log-normal distribution throughout and an approximately 13% increase in average [sub]grain diameter during the IAT.

When examined as a whole, the distribution plots in ***Figure 11*** also reveal that the IAT has resulted in a consistent movement in the peak position. This is indicative of an increase in the average [sub]grain area throughout the weld nugget cross-section. The tabulated data [inset] effectively highlights both the cross-sectional variation in, and the effect of the IAT on, the [sub]grain size. The dimensions are lowest at the A_R location, gradually increase toward 3t/4 and then decrease toward the R_C location. The most important finding is that the average [sub]grain area increases by approximately 30% across the entire weld nugget. Based on the $\pi.r^2$ relationship, this translates into a uniform increase in [sub]grain diameter of approximately 13%. The location of the finest (sub)grains at the A_R location may be significant, because it corresponds with the region which consistently contained the most AGG.

The uniform microstructural coarsening means that the slight grain size gradient documented is not modified by the IAT. This raises the question as to whether there is a change in the

associated (sub)grain boundaries which could make a supplemental contribution to AGG suppression. Further analysis of the EBSD data produced the statistical distribution of [sub]grain boundary misorientations along the AR-RC traverse shown in ***Figure 12***. Throughout the cross-section, the misorientation distribution differs from that of a randomly-oriented grain structure (21). As shown earlier for the A_R location [***Fig. 9(c)***], the distributions coincide at a boundary misorientation, θ ~ 30°. Above this value there are less HAGB's than random, and below it there are more boundaries, including LAGB's [θ<15°]. Dynamic RX, the presence of substructure, and retention of deformation-type texture components, are most likely responsible for this characteristic (20). Further, variations in the relative contributions of heat and work input during the FSW process may account for the different LAGB/HAGB ratio along the traverse (17).

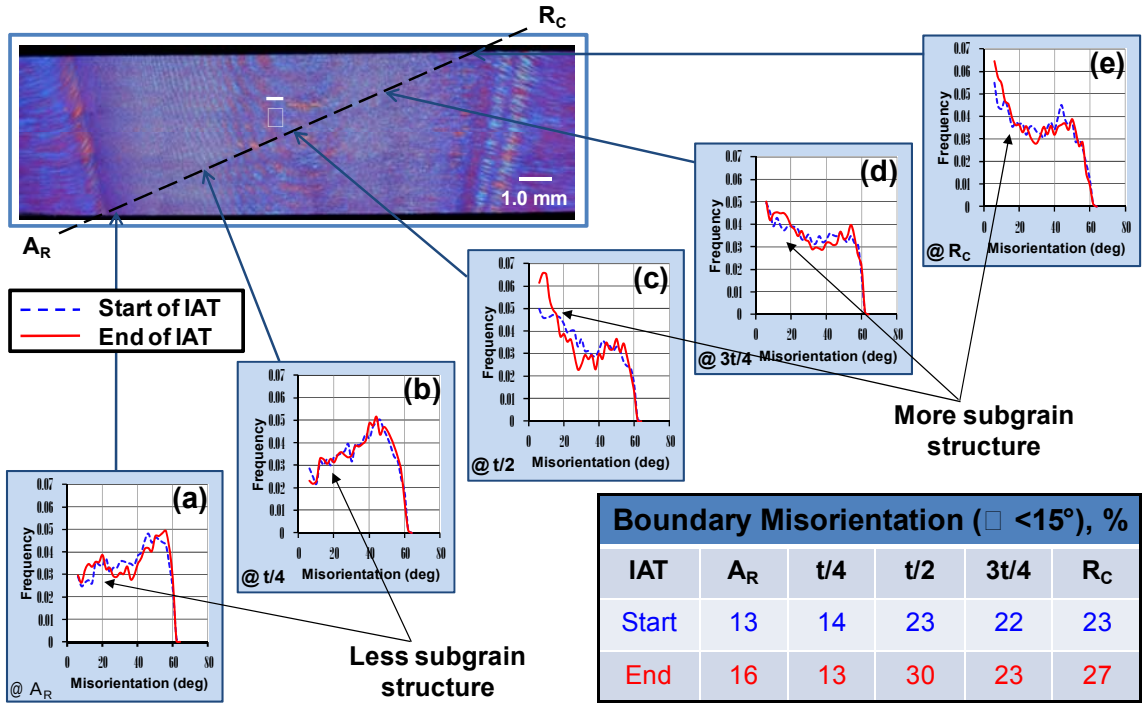

Boundary Misorientation (□ <15°), %					
IAT	A_R	t/4	t/2	3t/4	R_C
Start	13	14	23	22	23
End	16	13	30	23	27

Figure 12. Effect of IAT on [sub]grain boundary misorientation distribution along A_R-R_C traverse of deformed weld nugget: Figs.(a)-(e) show more LAGB's, and consequently less HAGB's, at A_R and t/4 locations. IAT causes subtle changes only.

Although the variations in the misorientation distribution along the traverse are not systematic, the data do indicate the presence of more HAGB's at A_R and t/4 [***Figs. 12(a) &(b)***], than at the t/2, 3t/4 and R_C locations [***Figs. 12(c), (d) &(e)***]. This may be interpreted as evidence that there is less subgrain structure on the advancing side and more on the retreating side of the weld nugget. Accordingly, the highest fraction of substructure appears to be at the t/2 location, where the frequency of LAGB's appears to be much larger [***Fig. 12(c)***]. This mid-weld region is coincident with the axis of the FSW tool and mass flow in this vicinity is likely to be the most complicated (18). As observed in ***Figure 7***, the bands of grains at this location exhibit a broad spacing and are horizontally inclined, unlike the t/4 location. Again, the onion rings may cause some data distortion due to sampling location and interpretation should be guarded (4). The tabulated data [inset] highlights both the cross-sectional variation in, and the effect of the IAT on, the frequency of subgrain boundaries [θ<15°]. A lower proportion of LAGB's at the A_R and t/4 locations with little change in frequency during the IAT is readily apparent. The existence of a higher proportion of HAGB's at the A_R to t/4 locations may be of significance. As mentioned earlier, this is the region of the weld nugget where AGG was observed to be the most persistent.

DISCUSSION

The insertion of an effective IAT into the dome processing schedule culminated in a significant reduction in the area fraction of oversized grains within the deformed weld nugget. The combination of FSW and SFD dictates that the microstructural condition in and around the nugget is complex. The abrupt transition between the nugget and the TMAZ at the advancing side, and the intersection of this interface with the root side of the weld result in very complicated characteristics. Current observations of AGG in the presence of a microstructural gradient are consistent with initiation within this region of highest stored energy, and the smallest grain size. In the 'SHT only' material condition, the oversized grains persisted at the A_R location during IAT development, ***Figs. 6(e)-(h)***. Therefore, variations in the primary driving force [reduction of stored energy] may be correlated with the changes in grain size across the weld nugget. The A_R location represents the region best-suited to initiation of AGG, with propagation along the resident gradient[s]. The use of diagonal traverses nugget during quantitative analyses offers an innovative perspective on how overall material flow is manifested in the microstructure of the weld nugget cross-section (20).

A synthesis of the microstructural changes resulting the IAT is presented in ***Figure 13***, which combines the tabulated data contained in ***Figures 10, 11, and 12*** in to two plots. ***Figure 13(a)*** shows the initial cross-sectional variations in microstructure, and a comparison with ***Figure 13(b)*** reveals the effect of the IAT on these microstructural characteristics. The [sub]grain diameter data suggests that the smallest grain size is at the A_R location. Comparing the two figures shows the ~13% increase in grain size across the whole weld nugget during the IAT. Although there are perturbations in grain diameter along the A_R - R_C traverse, a subtle upward gradient toward the R_C location is evident. This effect may be attributed to gradients in the mass flow, and varying heat/work input, characteristic of the FSW process, e.g. higher temperature correlates with larger grain size (20). The gradient persists following the IAT, which indicates that the microstructural coarsening affected was extremely uniform. The combined data are consistent with the growth advantage of isolated grains being mitigated by a reduction in the grain size differential with the surrounding array of grains (9). Whether a uniform increase in grain size of ~13% across the weld nugget is sufficient (in itself) to eliminate AGG is uncertain.

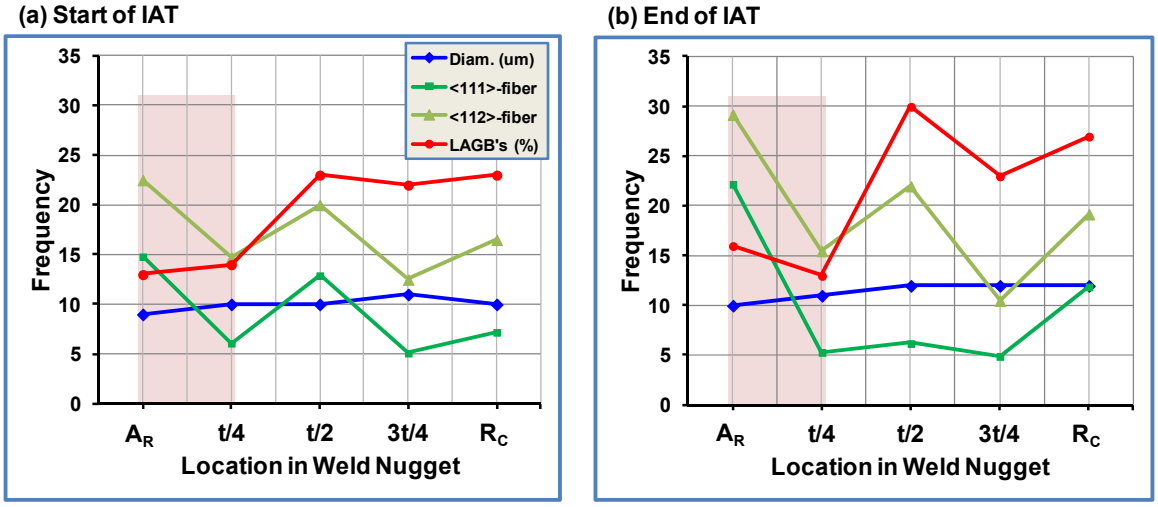

Figure 13. Graphical summary of tabulated data contained in Figures 10, 11, and 12, which can be correlated with [sub]grain size, orientation, and boundary misorientation variations across a deformed weld nugget: (a) beginning of the IAT: (b) conclusion of the IAT.

It is evident that the prime objective of promoting CGG at the expense of DGG has been achieved, and it may be inferred that the net driving force for AGG has been neutralized. The differential between driving and retarding forces was expected to be heterogeneous as a result of

the microstructural gradients observed through the cross-section. As mentioned earlier, the Alcan approach of increasing the particle-pinning effect of insoluble dispersoids on migrating grain boundaries was inapplicable (13). It is reasonable to assume that the primary source of retarding force, namely the highly stable Al_3Zr precipitates, would be unaffected by exposure to such low homologous temperatures (7). Any other retarding forces, such as those associated with soluble precipitates, would be expected to be homogenized across the nugget as a result of the IAT. The findings are inconsistent with an increase in retarding force contributing to AGG suppression at the A_R location. A pressing question remains; "Is there anything else that is different in the vicinity of the A_R location that could contribute to a reduction in the driving force for AGG ?", i.e. the shaded area on the plots in ***Figure 13***.

It is clear that the combination of FSW and SFD results in very complicated microstructural characteristics within the deformed weld nugget. The complex [sub]grain structure stems from the concurrent development of a strong deformation texture, and the occurrence of dynamic RX (6). During the IAT, the microstructure is further transformed by the prolonged exposure at a relatively high, recovery annealing temperature (8). As a consequence of uniform grain coarsening and no new grains emerging, it is not surprising that the overall textural composition across the weld nugget is relatively unaffected by the IAT (26). It also explains why the intensity of the <100> fiber [RX] is so weak at all locations, i.e. dynamic RX + recovery only. Of significance, is the apparent increased susceptibility to AGG at the A_R location, where the <111>- and <112>-fibers dominate the texture composition. The microtexture data shows that the contribution increases during the IAT, which indicates that annealing causes these deformation-type components to intensify. This is not unexpected because texture sharpening is commonly associated with recovery mechanisms, and the development of better-defined (sub)grain structures (6).

Consistent with previous work, the presence of the <111>-fiber suggests that the deformation behavior during FSW is similar to that which occurs during extrusion (17). It may be further inferred that there is a significant shear component oriented in the through-thickness direction [// S], due to helical mass flow (18). The presence of such a preferred texture accounts for some of the differences between the observed misorientation distributions and the traditional MacKenzie plot (21). The misorientation distribution data shows that the frequency of subgrain boundaries [$\theta<15°$] is lower at the A_R and t/4 locations, and also reveals only subtle changes during the IAT. In general, the microstructure comprises 80/20, HAGB's/LAGB's, which is unaffected by IAT. A higher frequency of LAGB's than random polycrystalline aggregate throughout the cross-section is not unexpected. Al-Li alloys are highly resistant to static recrystallization, and dynamic recrystallization tends to produce more subgrain structure (20). The observation of a change in the distribution of boundary misorientations within each of the two categories may be important.

The strong <111> fiber is probably related to the helical material flow around a rotating/ translating FSW tool, and the directionality of the associated shear deformation (17). The strong <112> fiber texture at the A_R location is not related to deformation by rolling, as is the case for the β-fiber (26). However, such a texture characteristic may result from the rigid body rotation of the idealized texture fibers associated with multi-directional shear deformation (20). That this should occur adjacent to the advancing interface is reasonable, based on the turbulent material flow envisioned in this vicinity during the FSW process (18). This may have provided additional impetus for the reaction to occur at the A_R location, but only in the as-formed condition. The microtexture data also suggests that some strengthening of the <111> and <112> fibers occurred during the IAT. It is possible that small changes in grain orientation can reduce the driving force for the AGG process by eliminating the growth advantage of isolated grains at the A_R location (9).

Crystallographic texture with a strong single component has been recognized as a driving force for DGG (6), but it may also act as a retarding force under the certain circumstances. For example, the effect of systematic texture gradients *per se* has yet to be determined. Furthermore, any influence of the periodic texture fluctuations associated with the onion ring features is likely to be more complicated. The onion rings can be associated with the 'advance

per revolution' characteristic of FSW processing and localized directionality of material flow (18). The resultant microstructural banding comprises grain orientation fluctuations created by transient shear deformation (17). The spacing between bands probably coincides with the level of shear deformation, which varies across the nugget. The rings are most evident between t/4 and 3t/4 in the cross-section because that is where the rotational contribution to material flow is considered to be highest (20). As the translational contribution increases toward the extremities of the nugget, the nature of the shear deformation involved becomes more complex. It is likely to be more severe on the advancing side, and reach a maximum adjacent to the TMAZ interface.

However, the extreme inclination of the onion rings at t/4 and 3t/4 may explain why the <110> fiber is so well-developed at these locations, i.e. mass flow dominated by multi-directional shear deformation [torsion] (22). Toward the lateral extremes of the FSW nugget, the translational contribution increases, with similarities to an extrusion (17). This is particularly true on the advancing side where the passage of the FSW tool results in severe deformation and creates an abrupt microstructural interface (18). This explains why the shear deformation textures are strongest in this region, i.e. conflicting rotational and translational contributions. It is reasonable to assume that the area of the microstructure that is the most heterogeneous would also be most susceptible to AGG. In this case, isolated grains with the largest growth advantage over the surrounding array are likely present in the vicinity of the A_R location.

The effects of the IAT on boundary misorientation distribution at the A_R location are subtle, and are presented in more detail in ***Figure 14***. As mentioned, the frequency of LAGB's is higher, and that of HAGB's lower than for a randomly-oriented array of grains (21). It was observed that the division between θ<30° and θ>30° boundaries was relatively unaffected by the IAT. However, the frequency of LAGB's [θ<15°] does seem to increase, which is consistent with the formation of substructure via recovery-type mechanisms during the IAT. Amongst the HAGB's [θ>15°], the frequency of 25-50° misorientations decreases and the frequency of 50-60° misorientations increases. It is widely accepted that certain types of grain boundary can migrate faster during recrystallization (6). Specifically, it has been documented that boundary misorientations close to the axis-angle pair relationship 40°<111> exhibit enhanced mobility in Al alloys (27). Therefore, these transitions may be evidence of an overall decrease in grain boundary mobility at the A_R location, and may have contributed to AGG suppression.

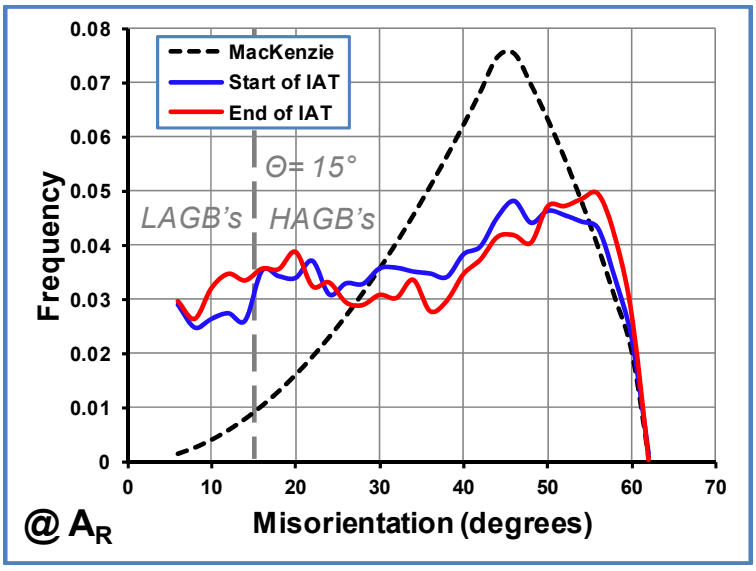

Figure 14. Effect of the IAT on [sub]grain boundary misorientation distribution at the A_R location. The overall distribution is different from a random distribution (21), but the two are coincident at θ ~30° The division between θ>30° and θ<30° boundaries is unaffected by the IAT, but the frequencies within the two categories undergo subtle changes.

SUMMARY

The fact that the material examined in this case study had been deformed after FSW, and only a partial weld nugget remained after SFD, presented a unique opportunity. Consequently, metallurgical analyses were conducted along a diagonal traverse of the much reduced cross-section, in order to effectively capture any gradient effects. Useful insight on the reduction in the net driving force for AGG was gained by quantifying microstructural differences between the start and end of the IAT, particularly at the A_R location. The current findings are consistent with modification of a dynamically recrystallized microstructure via CGG and recovery-type mechanisms.

The results presented suggest that the growth advantage of isolated grains can be negated by employing a simple, in-process IAT. Uniform microstructural coarsening within the deformed weld nugget, plus subtle changes in grain orientation and boundary misorientation, is deemed to be responsible. The proposed mechanism for the reduction in net driving force for AGG is a combination of factors, particularly as documented at the A_R location. This was the region of the deformed weld nugget where AGG was the most persistent during the thermal processing studies.

It is suggested that the first reduction in stored energy is by elimination of total boundary area, resulting from a measurable (~30%) increase in (sub)grain area. The second involves re-alignment of the grain structure (to a lower energy configuration), as evidenced by subtle shifts in microtextural composition. The third may involve a reduction in grain boundary mobility, as evidenced by the shift in the misorientation distribution of HAGB's. Individually, these contributions may not be sufficient to suppress AGG, but in combination they may exert a substantial influence. Returning to the concepts adopted for this case study (***Figs. 4, 5 & 8***), it may be assumed that the combined contribution will have a significant effect on the '$(M.\gamma/R)_A$ term' in the Humphreys model (9).

CONCLUSIONS

The application of a simple IAT to a friction-stir-welded and spin-formed Al-Li alloy 2195 material proved effective in suppressing AGG. The analyses suggest that uniform coarsening of a dynamically recrystallized microstructure was primarily responsible.

The approach combined microstructural stability concepts developed by Humphreys with gradient microstructure effects and traditional processing protocols. The objective was to promote CGG (during the IAT) to eliminate DGG (during SHT), i.e. suppress AGG.

AGG was most prevalent at the intersection between the advancing side [AS] and the root side of the deformed weld nugget. EBSD analyses revealed that this 'A_R' location exhibited the smallest grain size, strongest texture and highest frequency of HAGB's.

The most effective IAT caused an approximately 30% increase in (sub)grain area across the weld nugget. The subtle changes in grain orientations and HAGB misorientations accompanying the (sub)grain coarsening were consistent with CGG and recovery-type mechanisms.

First, the AGG threshold temperature was established, and second, the duration of a recovery annealing treatment below that temperature was determined. The processing philosophy adopted is applicable to many Al alloys scheduled for post-FSW deformation.

Insertion of a stand-alone IAT may allow for the cost effective manufacture of large, complex-shaped articles using single-piece forming operations. The current work implies that the size limitations on commercially-available stock can be overcome by using tailored starting blanks which have been friction stir welded together.

FUTURE WORK

Two of the objectives of future work will be;
(i) to categorize HAGB's in terms of coincident site lattice [CSL] boundaries, in order to establish whether overall mobility at the A_R location is affected by the IAT.
(ii) to evaluate the influence of soluble, second phase particles on grain boundary mobility, i.e. increased solute drag effects resulting from dissolution of precipitates during the IAT.

ACKNOWLEDGMENTS

The authors are very grateful to Joel A. Alexa and Harold D. Claytor of Lockheed-Martin Space & Science Division, Hampton, Virginia, for performing the processing work in the Light Alloy Laboratory at NASA Langley Research Center.

REFERENCES

1. ***Space Shuttle External Tank System Definition Handbook, Vols. 1 & 2***. LMC-ET-SE61-1. New Orleans, LA: Lockheed Martin Michoud Space Systems, December 1997.

2. Curreri, P.A, et al. ***Aluminum-Lithium, Friction Stir Welded, Spun-Formed Domes for Light-weight Cryogenic Propellant Tanks***. NASA/TP-11-216462. Huntsville, AL: Marshall Space Flight Center, March 2011.

3. Nelson, T.W., Steel, R.J., and Arbegast, W.J. ***Investigation of heat treatment on the properties of friction stir welds***. AeroMat 2001. Long Beach, CA: ASM International, June 2001.

4. Hales, S.J., and Tayon, W.A. ***Heat treatment of a friction-stir-welded and spin-formed Al-Li alloy***. Procedia Engng. 2011, Vol. 10, pp. 2496-2501.

5. Doherty, R.D., et al. ***Current issues in recrystallization: a review***. Mater. Sci. & Engng. 1997, Vol. A238, pp. 219-274.

6. Humphreys, F.J., and Hatherly, M. ***Recrystallization and Related Annealing Phenomena***. Second Edition. New York, NY: Elsevier, Ltd., 2004.

7. Hatch, J.E. [ed.]. ***Aluminum - Properties and Physical Metallurgy***. Metals Park, OH: ASM, 1984.

8. Rollett, A.D., Brahme, A.P., and Roberts, C.G. ***An overview of accomplishments and challenges in recrystallization and grain growth***. Mat.Sci.Forum. 2007, Vols. 558-559, pp. 33-42.

9. Humphreys, F.J. ***A unified theory of recovery, recrystallization and grain growth, based on the stability and growth of cellular microstructures - I. The basic model***. Acta Mater. 1997, Vol. 45, pp. 4231-4240.

10. Humphreys, F.J. ***A unified theory of recovery, recrystallization and grain growth, based on the stability and growth of cellular microstructures - II. The effect of second phase particles***. Acta Mater. 1997, Vol. 45, pp. 5031-5039.

11. Dennis, J., Bate, P.S., and Humphreys, F.J. ***Abnormal grain growth in Al-3.5Cu***. Acta Mater. 2009, Vol. 57, pp. 4539-4547.

12. Rioja, R.J. ***Fabrication methods to manufacture isotropic Al-Li alloys and products for space and aerospace applications***. Mat.Sci.& Engng. 1998, Vol. A257, pp. 100-107.

13. Ehrstrom, J.-C., and Warner, T. ***Manufacturing method for friction welded aluminum alloy parts***. US Patent 7,490,752 B2, February 17, 2009.

14. ***Heat treatment of wrought aluminum alloy parts***. AMS2770H. Aerospace Material Specifications. Warrendale, PA: SAE International, August 2006.

15. ***Standard test methods for determining average grain size***. ASTM E112 - 96. International Book of Standards. West Conshohoken, PA: ASTM, 2004. Vol. 03.01.

16. ***Practice for determining average grain size using electron backscatter diffraction (EBSD) in fully recrystallized polycrystalline materials***. ASTM E2627 - 10. International Book of Standards. West Conshohoken, PA: ASTM, 2010. Vol. 03.01.

17. Schnieder, J.A., and Nunes, A.C. ***Characterization of plastic flow and resulting microtextures in a friction stir weld***. Met.& Mat. Trans. 2004, Vol. 35B, pp. 777-783.

18. Fonda, R.W., Reynolds, A.P., et al. ***Material flow in aluminum friction stir welds***. Mater. Sci. Forum: Trans. Tech. Publ., Switzerland, 2012. Vols. 706-709, pp. 983-989.

19. Hassan, Kh.A.A., et al. ***Stability of nugget zone grain structures in high strength Al-alloy friction stir welds during solution treatment***. Acta Mater. 2003, Vol. 51, pp. 1923-1936.

20. Field, D.P., Nelson, T.W., et al. ***Heterogeneity of crystallographic texture in friction stir welds of aluminum***. Met. Mater. Trans. 2001. Vol. 32A, 11, pp. 2869-2877.

21. MacKenzie, J.K. ***Statistics associated with random disorientation of cubes***. Biometrika. 1958. Vol. 45, p. 229.

22. Hosford, W.S. ***The Mechanics of Crystals and Textured Polycrystals***. New York, NY: Oxford University Press, 1993.

23. Fonda, R.W., and Knipling, K.E. ***Texture development in friction stir welds***. Sci.& Tech. Welding & Joining. 2011, Vol. 16, 4, pp. 288-294.

24. Hales, S.J., and Hafley, R.A. ***Texture and anisotropy in Al-Li alloy 2195 plate and near-net-shape extrusions***. Mat.Sci.& Engng. 1998, Vol. A257, pp. 153-164.

25. Hales, S.J., and Hafley, R.A. ***Structure-property correlations in Al-Li integrally stiffened extrusions***. NASA/TP-2001-210839. Hampton, VA: Langley Research Center, April 2001.

26. Fricke, W.G., and Przystupa, M.A. ***Texture***. Aluminum Alloys - Contemporary Research and Applications. A.K. Vasudevan and R.D. Doherty (eds.). New York, NY: Academic Press, 1989, Vol. 31, pp. 563-578.

27. Huang, Y., and Humphreys, F.J. ***Measurements of grain boundary mobility during recrystallization of single-phase aluminium alloys***. Acta Mater. 1999, Vol. 47, 7, pp. 2259-2268.